Spin Nernst effect and spatiotemporal dynamic simulation of topological magnons in the antiferromagnet Cu_3TeO_6

Yizhi Liu [1], Chen Fang,[2,*] Shaoqin Jiang,[1] Yuan Li [1,3] and Limei Xu[1,3,4,†]

[1]*International Center for Quantum Materials, School of Physics, Peking University, Beijing 100871, China*
[2]*Beijing National Laboratory for Condensed Matter Physics, and Institute of Physics,*
Chinese Academy of Sciences, Beijing 100190, China
[3]*Collaborative Innovation Center of Quantum Matter, Beijing 100871, China*
[4]*Interdisciplinary Institute of Light-Element Quantum Materials and Research Center for Light-Element Advanced Materials,*
Peking University, Beijing 100871, China

The topological surface state arising from the nontrivial topology of the bulk band structure has attracted a wide range of interest. Compared with electrons, the magnon propagation in magnetic materials can be more intuitively reflected in the spin precession and generate different effects. Using molecular dynamics simulations, we study the real-space evolution of the magnon topological surface state in Cu_3TeO_6, a three-dimensional antiferromagnet with Dzyaloshinskii-Moriya interaction. We observe a coherent wave-packet propagation on the surface without attenuation into the bulk. As the intensity of the chiral Dzyaloshinskii-Moriya interaction increases, spin-dependent chirality of magnons appears on the surface. Such behavior suggests that Cu_3TeO_6 displays the magnon spin Nernst effect, i.e., the system generates a transverse net spin flow after applying a longitudinal temperature gradient. In our numerical calculations, when the intensity of the Dzyaloshinskii-Moriya interaction is about 10% of the nearest neighbor exchange interaction, the spin Nernst coefficient in this material is estimated to be around $\alpha_{yz} = 1\text{--}3 \times 10^{-16}$ J/mK.

I. INTRODUCTION

Over the past two decades, topological surface states (TSS) have attracted extensive attention and interest [1–6]. They are generally gap-closing edge modes that appear at interfaces between materials with different topological band structures [7–9]. Compared with normal surface states, topological edge modes are protected by the topology in momentum space. Therefore they are not affected by defects, irregular boundaries, or backscattering in real space as long as the symmetry is maintained. In particular, their band topology is independent of the statistics of the constituent particles, so novel transport can be realized in real systems. In fact, topological surface states have been proposed theoretically [10–19] and observed experimentally [1,2,20–24] in electronic systems such as topological insulators and topological semimetals [25–34].

In real space, TSS behaves as large-scale collective motions of particles or quasiparticles. In contrast to most studies of TSS in the momentum-frequency space [25–33,35], studies of TSS in real space-time, especially its dynamic evolution, is of great importance, as it can directly verify theoretical predictions and visualize transport properties of materials. In addition, complex interactions and surface defects within materials as well as their nonequilibrium evolution processes can also be better revealed. However, studies on the dynamic evolution of TSS are rather rare [36,37] and even less in real space-time $(\vec{r}, t)$.

Full quantum calculation is a straightforward approach to studying the real-time evolution of TSS, however, its high computational cost is an obstacle to its application in large systems. More precise techniques such as time dependent spin density functional theory [38], are applicable to describe dynamics but only within picoseconds and a few hundred atoms. Therefore a more effective method, such as semiclassical molecular dynamic (MD) simulations, is needed for large-scale collective motions of TSS in real space-time.

Recently, the concept of TSS has been further extended into bosonic quasi-particle systems such as photons [39,40], phonons [41], and magnons [42–47]. Compared with electrons, magnons (quanta of magnetic excitations) [48–51] are easier to visualize in real space because their wave function corresponds directly to the spin of ions in real space. In addition, magnons (neutral bosonic quasiparticles) have different transport properties from electrons, such as long-distance propagation without being affected by Lorentz forces and Joule heat in magnetic materials. Therefore studying the transport properties of magnons is of great significance for magnetic materials and spintronics.

Cu_3TeO_6 is a Mott insulator that exhibits antiferromagnetic order below the Neel temperature ($T_N = 61$ K) [47,52–54]. The arrangement of spin-1/2 on the Cu^{2+} sublattice in this antiferromagnetic order is predominantly collinear and bipartite, as shown in Fig. 1. It has a rich topological magnon band structure, thus is a convenient playground to study the topological magnon surface states [47,55]. In particular, quantum fluctuations in Cu_3TeO_6 are suppressed by far-reaching

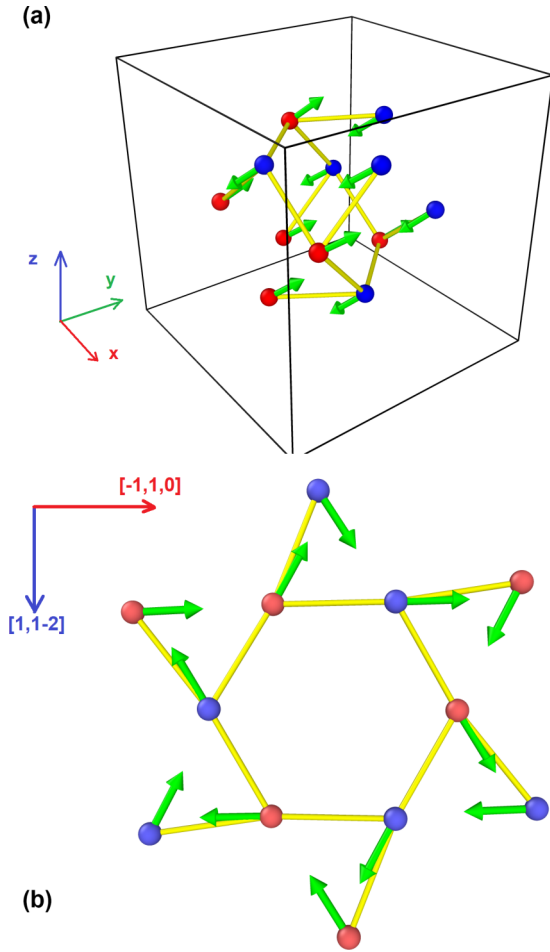*cfang@iphy.ac.cn
†limei.xu@pku.edu.cn

FIG. 1. (a) Illustration of the ground state in the primitive cell of Cu_3TeO_6 for $D_m = 0.25J_1$. The green arrow indicates the spin. (b) shows the layer structure and the component of the spin in the plane perpendicular to the [111] direction (amplify 25 times). Spin-up and spin-down Cu^{2+} are denoted by the red and blue circles, respectively. The yellow line between two Cu^{2+} represents the nearest neighbor at a distance of $r = 0.318$ nm.

interactions [47], allowing them to be studied in a semiclassical manner. Recently, based on the Heisenberg model and neglecting the contribution from the Dzyaloshinsky-Moriya interaction (DMI), Yao *et al.* [47] obtained the Hamiltonian of the system,

$$H_H = J_1 \sum_{\langle ij \rangle} \mathbf{S}_i \cdot \mathbf{S}_j + J_2 \sum_{\langle\langle ij \rangle\rangle} \mathbf{S}_i \cdot \mathbf{S}_j + \cdots + J_9 \sum \mathbf{S}_i \cdot \mathbf{S}_j,$$

(1)

where $J_1, \ldots, J_9$ are exchange interactions obtained by fitting the inelastic neutron scattering data. However, when the bond angle of the Cu-O-Cu bond is less than $180°$, the DMI generally exists between two nearest Cu^{2+} neighbors. So the contribution of the DMI, H_{DMI}, to the Hamiltonian H,

$$H = H_H + H_{DMI} = H_H + D_m \sum_{\langle ij \rangle} \hat{\mathbf{d}}_{ij} \cdot \mathbf{S}_i \times \mathbf{S}_j, \quad (2)$$

can be of significance. Here D_m is the intensity of the DMI [56,57] and $\hat{d}_{ij}$ is the normal direction of the triangle made

from the Cu–O–Cu bond. H_{DMI} term is the origin of chiral interactions in Cu_3TeO_6, which provides a natural explanation for the ground state spin orientation along the [111] direction that cannot be explained by the Heisenberg model [55]. We note that the strength of DMI in this material has been controversial [43,52,55,58]. For instance, first principles calculations suggested that the DMI in Cu_3TeO_6 are rather weak, $D_m = 0.06J_1$, where J_1 is the nearest neighbor exchange interaction [43]. However, the experimental study showed that the canting angle of the spins from the [111] direction is of the order of $6°$ [52], corresponding to $D_m = 0.2J_1$ [47]. In a recent experiment, by calculating the magnetization with different external magnetic fields, the DMI in Cu_3TeO_6 is refined to be $D_m = 0.1J_1$ [58].

We thus investigate a possible range of these DMIs ($D_m = 0.0 - 0.30J_1$). Using classical molecular dynamics (MD) simulations and linear spin wave theory (LSWT), we study the transport properties of topological magnon surface states of Cu_3TeO_6 in momentum space and real space. A coherent wave-packet propagation of the topological surface states, the magnon wave packet, is observed on the surface without attenuation into the bulk state for the entire range of D_m investigated.

However, the characteristics of the band structure and the way of magnon wave-packet propagation are different without ($D_m = 0$) or with ($D_m > 0$) the DMI terms. In the case of $D_m = 0$, the ground state is a collinear antiferromagnet. For any given state (magnon), there is always another one with the same spin but opposite propagation direction on the same surface, so the total spin current and the energy current generated by the magnons are always 0. In contrast, when $D_m > 0$, H_{DM} term in Eq. (2) introduces chirality into the system, thus breaking the collinearity of the ground state. As a result, spin-up and spin-down magnons move in opposite directions on a single surface, thereby generating two net spin currents on the upper and lower surfaces.

The above features can be explained in terms of symmetries. When $D_m = 0$, the system is invariant under time reversal followed by a spin rotation of $180°$ along the spin y-axis transformation [$R_y(180°) * T$ symmetry], which enables the symmetric backward propagation of a magnon with the same spin on a single surface. When $D_m > 0$, this symmetry is broken and introduces chirality to the system, resulting in a nonzero net spin current on single surfaces. In both cases, the system has the PT (time reversal followed by space inversion) symmetry, which guarantees that the net spin currents on the upper and lower surfaces are of the same magnitude and direction, but with opposite spins. Thus, when a longitudinal temperature gradient is applied across the upper and lower surfaces, a transverse net spin current can be generated. This indicates that considering the DMI, Cu_3TeO_6 displays the magnon spin Nernst effect [59,60] (SNE).

In a recent experiment, the intensity of DMI is refined to be $D_m = 0.1J_1$ in Cu_3TeO_6 [58]. We calculate the SNE coefficient for $D_m = 0.1J_1$ in this material and find that depending on the experimental temperature, α_{yz} varies from 1×10^{-16} to 3×10^{-16} J/mK. This work elucidates the surface state properties of Cu_3TeO_6 in the presence of DMI and predicts the SNE effect, which is useful for future experimental and theoretical investigations in Cu_3TeO_6.

The rest of the manuscript is organized as follows, Sec. II contains the calculation details, Sec. III discusses the characteristics of bulk band structures based on LSWT calculation and MD simulations, and Sec. IV presents the calculation results of topological surface state in momentum space and real space. In Sec. V, the SNE coefficients of the system are shown; and finally, a summary is concluded in Sec. VI.

II. METHOD

To calculate the surface band structure in Cu_3TeO_6, we build slabs consisting of N_i ($N_i = 10, 30, 50$) lattices stacked in the z direction. They have two free boundaries in the z direction and are periodical in the x-y plane. Then, the surface band structure is studied using LSWT. Since the surface states are barely affected by size effects (see Fig. S4 in Ref. [61]), a slab of ten-layer lattices is used in the main text. To ensure the generality of the results, two geometrically different surfaces were cut along the [001] direction. In fact, topological surface arc states always exist no matter how they are cut, although their shape in the surface BZ depends on the geometry of the surface (see Figs. S5 and S6 in Ref. [61]). Moreover, our conclusions or the physical mechanisms involved are not affected by surface geometries.

The dynamic evolution of magnon surface states was studied using semiclassical molecular dynamics (MD) simulations [62–64] on a slab of $80a \times 80a \times 10a$ (1 561 600 Cu atoms). Here $a = 9.537$ Å is the lattice constant. All simulations are performed at $T = 0$ K to eliminate any thermal fluctuation or lattice vibration. The free boundary in z direction and periodic boundary conditions in x and y directions are applied. Note that the MD simulations are carried out on LAMMPS [65] with SPIN package included [66].

To calculate the SNE coefficient, a steplike temperature gradient is applied to the Cu_3TeO_6 slab. The slab is uniformly divided into five layers along the z direction with an assigned temperature T_i ($i = 1, 2, 3, 4, 5$) for each. The temperatures satisfy $T_1 < T_2 < T_3 < T_4 < T_5$, and $T_5 - T_1 = \Delta T \rightarrow 0$ to ensure a linear dependency. Bose distribution is used to describe the probability of one magnon excitation in each layer, $\rho(E_{n\mathbf{k}}; T_i) = 1/[\exp(E_{n\mathbf{k}}/k_B T_i) - 1]$, where $E_{n\mathbf{k}}$ is the energy of Bloch wave function $|\phi_n(\mathbf{k})\rangle$ in the nth magnon band at $\mathbf{k}$ in 2D BZ. The spin current on the surfaces (x-y plane), contributed by eigenstate $|\phi_{n\mathbf{k}}\rangle$, is calculated according to

$$\mathbf{j}_x^n = \frac{1}{V} \sum_{k,i} \mathbf{S}_i^n \cdot \rho(E_{nk}; T_i) \frac{1}{\hbar} \frac{\partial E_{nk}}{\partial kx},$$

$$\mathbf{j}_y^n = \frac{1}{V} \sum_{k,i} \mathbf{S}_i^n \cdot \rho(E_{nk}; T_i) \frac{1}{\hbar} \frac{\partial E_{nk}}{\partial ky}, \quad (3)$$

where V is the volume of the system, i represents the ith layer of the slab, $\mathbf{j}_x^n$, $\mathbf{j}_y^n$, $\mathbf{S}_i^n$ are 1×3 vectors representing the component of spin in the x, y, and z directions, and $\frac{1}{\hbar} \frac{\partial E_{n\mathbf{k}}}{\partial ky}$ is the group velocity. Then the SNE coefficient is calculated according to

$$j_i^s = -\alpha_{ij}^s \frac{\partial T}{\partial z}, \quad (4)$$

where j_i^s represent the spin current in [111] direction, i and j represent the xyz component, and α_{ij}^s is the lateral spin current at a unit temperature gradient [59,60,67,68]. Note that the [111] direction is defined as the z direction of the spin space, that is, the spin along the [111] direction is spin-up and the spin along the $[-1-1-1]$ direction is spin-down.

III. BULK BAND STRUCTURE

Based on the effective Hamiltonian in Eq. (2), we gradually tune the DMI by varying intensity D_m from 0 to $0.30J_1$, to investigate how the ground state and magnon band structure are affected. The ground state is calculated from molecular dynamic (MD) simulations, and the magnon band structure was calculated using linear spin wave theory (LSWT).

Strikingly, semiclassical MD simulations well reproduce previous results for $D_m = 0$. The antiferromagnet ground state is a collinear arrangement of 12 Cu^{2+} ions in the primitive cell, and in the magnon band structure [Fig. 2(a)], there are six double degenerate bands with three Dirac points at P. Two of them are very close around $E = 15$ meV, and the other is at $E = 17.6$ meV. In contrast, when $D_m > 0$, the original collinear ground state at $D_m = 0$ is no longer the lowest energy state, thus losing its stability. Instead, a noncollinear state with a slightly tilted spin direction becomes the ground state. The tilting angle, defined as the angle between the spin direction and the [111] direction, is proportional to D_m. Meanwhile, the band structure of Cu_3TeO_6 obtained from the LSWT calculations for $D_m > 0$ (e.g, $D_m = 0.25J_1$) is also different from that for $D_m = 0$. As can be seen from Fig. 2, the original six double degenerate bands [Fig. 2(a)] are split into 12 independent bands [Fig. 2(b)], and the Dirac point at $E = 17.6$ meV expands into a nodal line [red line, Fig. 2(b)] along the [111] direction (P-Γ path), whose length is proportional to D. Specifically, from P to Γ, four energy bands become three, forming a double degenerate line along the path. In addition, a small energy gap is also opened at the bottom of the "acoustic" branch (see Fig. S1 in Ref. [61]). This energy gap as a function of D_m, shown in Fig. 2(c), is well fitted by a quadratic function of D_m, $E = aD_m^2$ with $a \approx 0.91$. Once E is obtained from the magnon band structure experimentally, D_m can also be determined, thus providing a way to estimate the DMI intensity. We note that the energy gap induced by DMI (about $E = 0 - 0.08$ meV) is much smaller than that estimated from the INS experiment (about 2 meV) [47]), suggesting that it is not the DMI but other anisotropic interactions are responsible for the energy gap of 2 meV. However, these changes are difficult to be observed experimentally due to the resolution (see Fig. S2 in Ref. [61]), though the inclusion of DMI does bring changes in the band structures. This is why the Spin Nernst coefficient is a convenient quantity to estimate the strength of DMI.

In general, global U(1) spin-rotation symmetry exists in most collinear antiferromagnets, and PT (time reversal followed by space inversion) symmetry pertains to various antiferromagnets with centrosymmetric crystal lattices. These two symmetries make the spin wave Hamiltonian block-diagonalized ($H = H_+ \oplus H_-$) under the standard Holstein-Primakof transformation and satisfy $H_+ = H_-^*$. So the magnons on the spin-up (H_+) and spin-down (H_-)
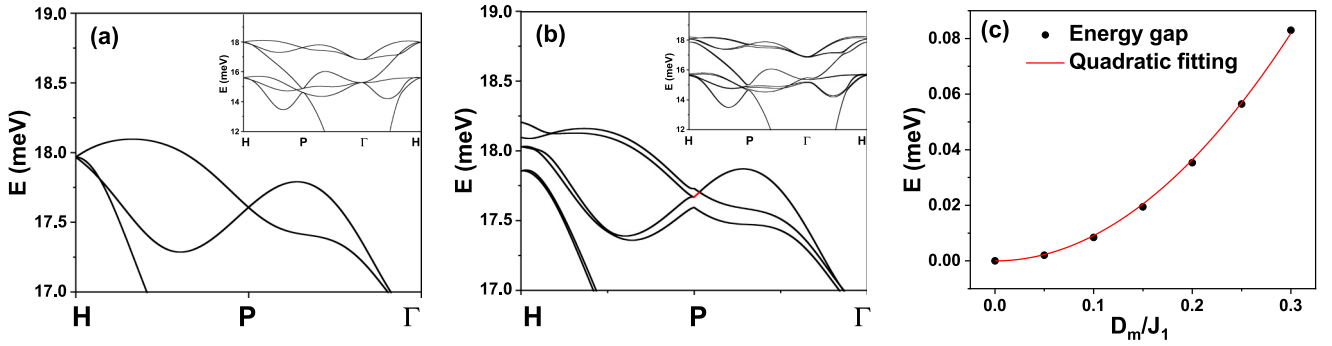
FIG. 2. Bulk band structure of magnon dispersion for (a) $D_m = 0.0$ and (b) $0.25J_1$ along high symmetry lines near the Dirac point at P ($E = 17.6$ meV). Bulk band structures of magnon dispersion for $E > 12$ meV along H-P-Γ-H are shown as the inset. The red line represents the nodal line for $D_m = 0.25J_1$. (c) The size of the energy band gap at the bottom of the "acoustic" branch at P as a function of DMI intensity D_m, which is well fitted by a quadratic function (red line).

sublattices are decoupled and symmetric, which explains why each eigenstate in the Brillouin zone is at least doubly degenerated [Fig. 2(a)], with one spin-up and the other spin-down.

In contrast, when introducing the DMI ($D_m > 0$), the ground state becomes noncollinear, and the spin rotation U(1) symmetry is broken, resulting in the splitting of the original 6 degenerate bands [Fig. 2(a)] into 12 independent ones [Fig. 2(b)]. It is also important to stress that the threefold rotation symmetry along the [111] axis ($C3$ group) and the PT symmetries still remain even when the DMI is introduced ($D_m > 0$). The $C3$ group has three one-dimensional representations, two of which are mutually conjugate. Due to the PT symmetry, the wave functions are conjugate, and spins can be reversed, so the two one-dimensional representations are degenerate. It is due to the preservation of $C3$ (threefold rotation along the [111] axis) and PT symmetries that the Dirac point expands into a nodal line along the [111] direction [red line, Fig. 2(b)].

Here we note that the symmetry-based considerations we used to explain magnon surface effects and Dirac points are not only for 0 K. To show the temperature effects, we also calculate the spin dynamical correlation functions [69] in finite temperature (see Fig. S2 in Ref. [61]). But since the topological energy bands are located in the high energy regions ($E > 12$ meV) and require higher temperatures to be effectively excited, increasing the temperature does not affect the topological band structures in high energy.

IV. TOPOLOGICAL SURFACE STATE

Considering DMI, the topological magnon band structure of Cu_3TeO_6 obviously becomes much richer. According to the bulk-edge correspondence principle [7–9], two materials with different topological band structures must undergo gap-closing edge modes at the interface. In the following, we investigate the magnon surface band structure of a ten-layer Cu_3TeO_6 slab using LSWT.

The ground state of the Cu_3TeO_6 slab is investigated using molecular dynamic (MD) simulations for the first time. It is found that the ground state remains a collinear antiferromagnet for $D_m = 0$, but changes to noncollinear near [111] direction with a tilting angle for $D_m > 0$. MD simulations also

show that the tilting angle is more prominent on the surfaces when introducing the DMI.

The eigenstates of the slab near the Dirac point ($E = 17.6$ meV) in a two-dimensional (2D) BZ for $D_m = 0$ and $0.25J_1$ are presented in Fig. 3. As can be seen, there are eight surface-arc states in the 2D BZ. They can be further divided into four groups according to their total spin ($+1$, -1, or 0) and spatial location (upper or lower surface), namely, (i) spin-up on the upper surface with $S_{upp} \approx 1$ and $S_{low} \approx 0$ (red points), (ii) spin-down on the upper surface with $S_{upp} \approx -1$ and $S_{low} \approx 0$ (blue points), (iii) spin-up on the lower surface with $S_{upp} \approx 0$ and $S_{low} \approx 1$ (yellow points), and (iv) spin-down on the upper surface with $S_{upp} \approx 0$ and $S_{low} \approx -1$ (cyan points). The bulk states are colored green. Note that S_{upp} and S_{low} represent the spin on the upper and lower surfaces, respectively. Previous study [10] showed that surface dispersion is topologically equivalent to a double-helicoid structure centered at the projection of the Dirac point [10] when two bulk bands cross at a Dirac point, and its isoenergy plane intersects the double-helicoid at the energy corresponding to the Dirac point, forming two arcs from the projected Dirac point. Likewise, the eight surface-arcs for $D_m = 0$ in Fig. 3(a) originated from the projection of P ($1/2, 1/2$) onto the 2D BZ and associated with the fourfold degenerate Dirac point of the bulk band structure at $E = 17.6$ meV. The surface dispersion for $D_m > 0$, however, becomes much more complicated [Fig. 3(b)]. For instance, the Dirac point becomes a nodal line that displays a drumheadlike surface state structure, which is beyond the scope of our study. Here we mainly focus on the eight arcs.

The group velocity direction through energy gradient is then investigated for the eigenstates on the arcs on the upper surface. Taking the states A, B, C, and D shown in Fig. 3 as an example, which corresponds to the states with spin-down propagating along (x, y) direction, spin-down along $(-x, -y)$, spin-up along $(x, -y)$, and spin-up along $(-x, y)$ directions, respectively. It is found that the arc eigenstates (A/C and B/D) at $\vec{k}$ and $-\vec{k}$ with the same spin are always symmetric for $D_m = 0$ [Fig. 3(a)] but become asymmetric for $D_m > 0$ and also have group velocities different from those for $D_m = 0$.

To visualize the transport characteristics of the magnon surface states of the slab, we construct an initial configuration
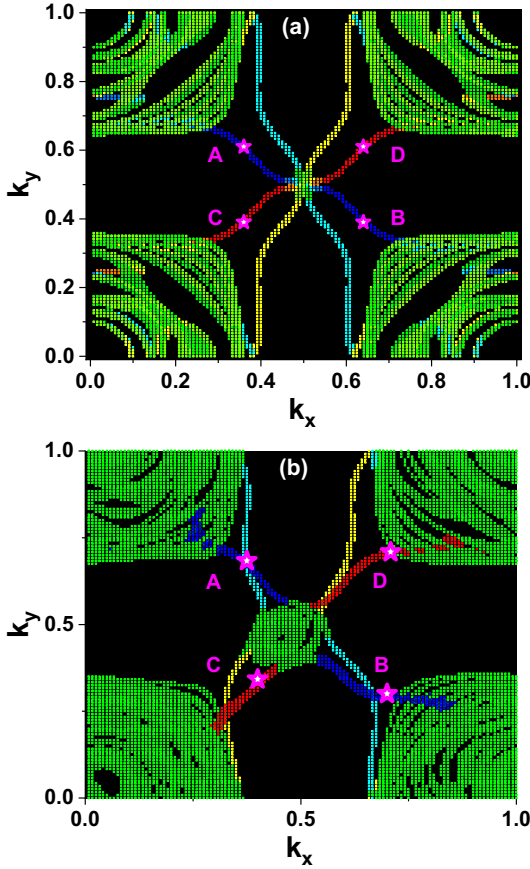
FIG. 3. Eigenstates of ten-layer Cu_3TeO_6 slab (240 atoms) at $E = 17.6 \pm 0.002$ meV in two dimensional Brillouin zone for $D_m = 0$ (a) and $D_m = 0.25J_1$ (b). There are eight surface arcs emanating from the projection of Dirac point (0.5,0.5) for $D_m = 0$. The total spins of a magnon on the upper (S_{upp}) and lower (S_{low}) surfaces are colored according to their values. Precisely, spin-up on the upper surface with ($S_{upp} \approx 1$, $S_{low} \approx 0$), spin-down on the upper surface with ($S_{upp} \approx -1$, $S_{low} \approx 0$), spin-up on the lower surface ($S_{upp} \approx 0$, $S_{low} \approx 1$), and spin-down on the upper surface ($S_{upp} \approx 0$, $S_{low} \approx -1$) are colored in red, blue, yellow, and cyan, respectively. The bulk states ($S_{upp} \approx 0$, $S_{low} \approx 0$) are colored in green. A, B, C, and D are four characteristic surface arc states on the upper surface with spin-up propagating along (x, y) spin-up along $(-x, -y)$, spin-down along $(x, -y)$, and spin-down along $(-x, y)$ directions when $D_m = 0$, respectively. The wave-packet propagation of A/C and B/D are always symmetric for $D_m = 0$ due to the existence of $R_y(180°) * T$ symmetry, while it becomes asymmetric when $D_m = 0.25J_1$ due to symmetry breaking.

of the ground state and add wave packets of the magnon. The magnon wave packet is the superposition of the four eigenstates (A, B, C, D) on the four Fermi arcs on the upper surface with $E = 17.6$ meV, multiplied by the Gaussian function. Subsequently, the dynamic evolution of the magnon wave packets is simulated using semiclassical molecular dynamics (MD) simulations. The result is presented in Fig. 4. The intensity of spin deviation is defined as $I_i = |S_i - S_{i,0}|^2$, where $S_{i,0}$ and S_i represent the spins of the excited and ground states of the ith Cu^{2+} ion. Intensities for spin-up and spin-down are represented by the blue and red arrows, respectively.

As can be seen from Fig. 4, the wave packet propagates on the surface of Cu_3TeO_6 slab (black squares). For $D_m = 0$, the topological surface state wave packages of A/C and B/D are always symmetric [Figs. 4(a)–4(d)], with the same magnitude and spin but opposite directions (group velocity direction) of propagation. This is consistent with the results calculated by LSWT. In contrast, for $D_m > 0$, wave packets of B/D propagate away from their original directions over time and are no longer symmetric with those of A/C [Figs. 4(e)–4(h)]. To be more specific, when $D_m > 0$, the spin-up wave packet of B moves to the left, and the spin-down wave packet D moves to the right with respect to the propagation direction of wave packets for $D_m = 0$, thereby magnons carrying spin-up and spin-down move in entirely different directions on a single surface.

Furthermore, topological magnon surface states can propagate coherently on the surface without decaying toward the bulk states (see Fig. 4). This is manifested by the dynamic evolution of the distribution of magnon in the z direction. As can be seen from Fig. S2 in Ref. [61], within a simulation time of 160ps, 98% of the spin excitation is distributed on the surface ($z > 8a$) and does not decay with time, while only 2% spin excitation is located between the surface and the bulk state ($6a <= z <= 8a$).

The above characteristics of the surface arc state can be understood by the fact that the $R_y(180°) * T$ symmetry is preserved for $D_m = 0$ and broken for $D_m > 0$. For the $R_y(180°) * T$ symmetry, $R_y(180°)$ rotates the spin 180° around $y-axis$ and T is the time reversal operation that inverses the spin, that is, $(Sx, Sy, Sz, t) \rightarrow (Sx, -Sy, Sz, -t)$. In the case of $D_m = 0$, under the $R_y(180°) * T$ symmetry, the momentum of a single magnon is reversed but the spin in [111] direction (S_z) remains unchanged. Thus, for a given state at $\vec{k}$, there is always a symmetric state at $-\vec{k}$ with the same spin (S_z). So the total spin current and energy current are always 0 on a single surface. However, in the case of $D_m > 0$, the DMI breaks this symmetry, resulting in the asymmetric propagation of A and C such that summing all spin-up magnons produces a net spin-up current (same for spin-down). We also note that for $D_m > 0$, the magnons on a single surface exhibit spin-dependent chirality, with the spin-up and spin-down magnons shifting in opposite directions. Briefly, the $R_y(180°) * T$ symmetry enables the magnon of the same spin on the surface to generate a current, and the chirality of the DMI causes the currents with spin-up and spin-down to propagate in opposite directions. Therefore, when $D_m > 0$, a nonzero pure spin current exists on a single surface.

Actually, under PT symmetry, the spin current discussed above on a single surface is correlated with that on the other surface. Considering an ideal case that the upper and lower surfaces are symmetric (see Fig. S4 in Ref. [61]) and the PT symmetry is preserved, the spatial inversion operation transfers the spin current on the upper surface to the lower surface and the time reversal operation reverses its spin, while the propagation direction remains unchanged after both operations. So the total spin currents generated on the upper and lower surfaces have the same magnitude and direction but opposite spins due to the PT symmetry, leading to the spin Nernst effect (SNE), we discuss next.
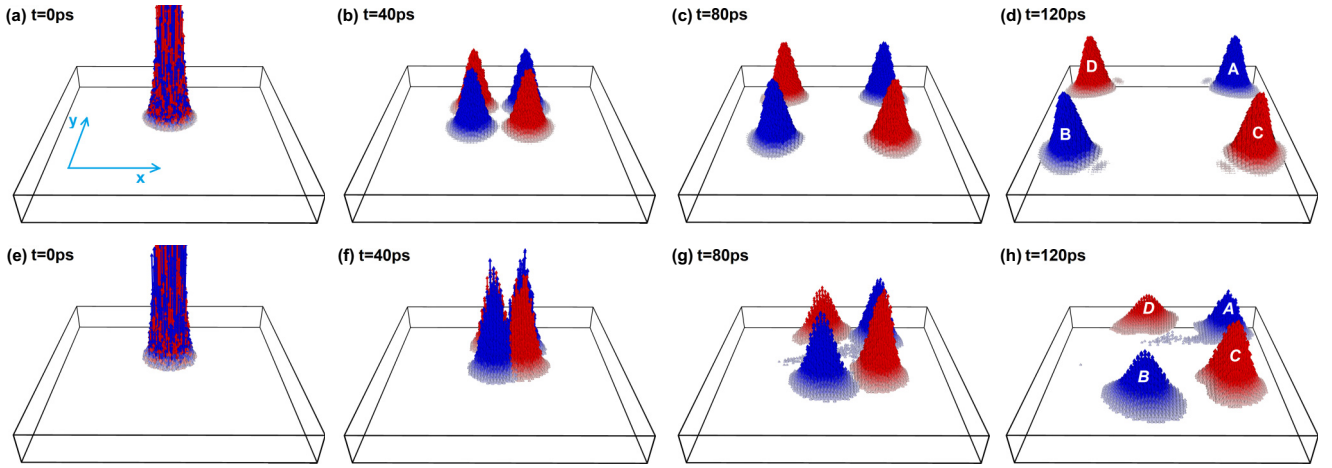
FIG. 4. Dynamic evolution of topological magnon surface wave packets composed of surface arc states $A - D$ for $D_m = 0.0$ [(a)–(d)] and $D_m = 0.25J_1$ [(e)–(h)]. The vector represents the magnitude of the spin deviation from that in the ground state, $I = |S - S_0|^2$. Spin-up and spin-down are colored in red and blue, respectively, and shades of color represent intensity. When $D_m = 0$, the wave packets of A/C and B/D are always symmetric. However, when $D_m > 0$, the wave-packet propagation of A/C deviates from their original direction.

V. SPIN NERNST EFFECT

According to previous discussions, when a longitudinal temperature gradient is applied along the z direction, magnons on the two surfaces can be excited with different probabilities, resulting in transverse spin currents in x and y directions ($\mathbf{j}_x^s$ and $\mathbf{j}_y^s$). This indicates that Cu_3TeO_6 has the spin Nernst Effect (SNE). We calculate the SNE coefficient α_{xz}^s and α_{yz}^s of Cu_3TeO_6 according to Eq. (3) and present the result in Fig. 5. For $D_m = 0$, $\alpha_{yz} = 0$ at all temperatures, that is, due to the $R_y(180°) * T$ symmetry, the surface magnons always have zero contribution to the spin current. The magnitude of α_{yz} increases monotonically as D_m and T increase [Fig. 5(a)], which can be experimentally measured conveniently. For instance, for $D_m = 0.2J_1$ and $T = 50$ K, $\alpha_{yz} \approx -5 \times 10^{-16}$, corresponding to a transverse spin current of about 10^{-11} J/m^2 at a temperature gradient of 20 K/mm [67,70,71]. The behavior of α_{xz} is rather complicated, and the SNE coefficient in the x direction is an order of magnitude smaller than in the y direction [Fig. 5(b)].

In the bulk state, $C3$ symmetry (threefold rotation along the [111] axis) guarantees that our system is invariant under $(x, y, z) \rightarrow (y, z, x) \rightarrow (z, x, y)$ transformation. It means that the bulk state is equivalent in the x, y, and z directions. Due to the lack of $C3$ symmetry on the surface of Cu_3TeO_6, the SNE coefficient behaves differently in the x and y directions. The SNE coefficient in the x direction first decreases and later increases, mainly due to the competition between trivial surface states (at $E < 12$ meV) and topological surface states (at $E > 12$ meV). In contrast, the trivial surface states contribute little to the total spin current in the y direction (because they always tend to cancel with each other), leading to the transport properties of the topological surface states in the y direction being more significant (see Fig. S9 in Ref. [61]).

The experimental measurement of the SNE coefficient is usually done by converting the spin current into a charge current through the inverse spin Hall effect (ISHE), that is, attaching a strong spin-orbit coupled metal layer to the antiferromagnetic material. As a result of the spin-orbit coupling, electrons with opposite spins move in opposite directions as the spin current enters the metal layer, creating a voltage that can be measured. It is reported that the transverse spin current is the order of 10^{-10} J/m^2 at a temperature gradient of 20 K/mm in typical three-dimensional systems [67,70,71]. Compared with that of other substances [67,68],
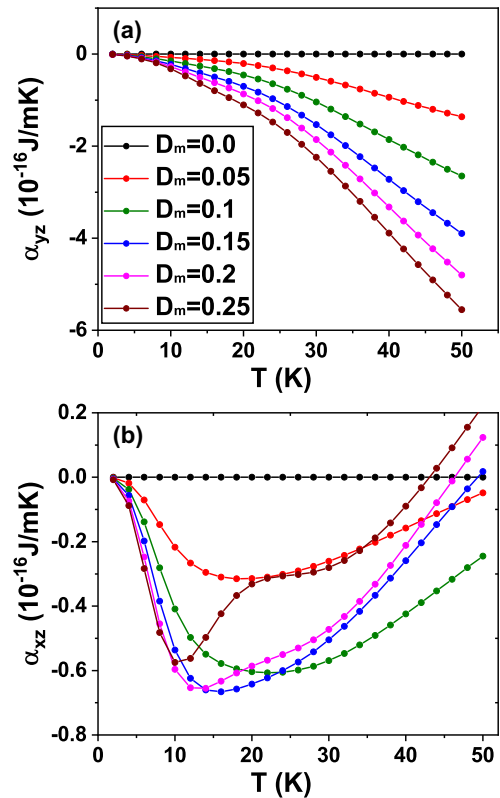

FIG. 5. Spin Nernst coefficient/conductivity in three dimensions Cu_3TeO_6 slab along (a) y and (b) x directions as a function of temperature for different DMI intensity D_m. The temperature range is below the Neel temperature (61 K).

the SNE effect of Cu_3TeO_6 is not very significant. This is because the topological surface states are distributed in the high energy region ($E > 12$ meV), which requires higher temperatures to be excited. An alternative way to enhance the SNE coefficient in Cu_3TeO_6 is to increase the chemical potential to excite more topological surface states in high energy regions.

It is important to note that the contribution of the lateral spin current is almost from the surface states, whereas the overall contribution of magnons in bulk is nearly zero due to the PT symmetry. Given these characteristics, Cu_3TeO_6 can be used to fabricate spintronic devices. For example, if the sample is thick enough that the lower surface is no longer important, then a "thermal diode" or "thermal check valve" can be fabricated from the upper surface [72–74].

We further note that magnons in Cu_3TeO_6 barely contribute to the thermal Hall effect, a phenomenon that produces a lateral heat current when a longitudinal temperature gradient is applied to the system. This is because the total spin-up and spin-down currents in Cu_3TeO_6 coexist but move in opposite directions. Therefore the contributions of magnons with different spins to the heat flow cancel out, leading to no magnon thermal Hall effect. Our analysis is also consistent with recent experiments in which the magnon contribution to thermal hall conductivity was excluded in Cu_3TeO_6 [75].

VI. SUMMARY

To summarize, using linear spin wave theory and molecular dynamic simulation, we investigate the topological magnon surface states in Cu_3TeO_6 with the Dzyaloshinskii-Moriya interaction intensity D_m varying from 0 to $0.30J_1$. It is found that for all the ranges of D_m investigated, the topological surface states propagate coherently without attenuation into the bulk state. However, the way of propagation is different with or without the Dzyaloshinskii-Moriya inter-action. When $D_m = 0$, due to the $R_y(180°) * T$ symmetry, symmetric topological surface states with the same spin and opposite propagation direction exist on a single surface, so the total spin current of the system is 0. In contrast, when $D_m > 0$, the Dzyaloshinskii-Moriya interaction breaks the $R_y(180°) * T$ symmetry, causing the magnons with opposite spins to move in opposite directions. Such asymmetric propagation of the magnons results in the emergence of a net spin current on a single surface. Furthermore, due to the PT symmetry, the net spin current generated on the upper and lower surfaces has the same direction but carries opposite spins. Thus, when a longitudinal temperature gradient is applied, the magnons on the upper and lower surfaces can be excited with different probability and a transverse spin current emerges, known as the magnon spin Nernst effect. Our study clearly demonstrates the collective behavior of topological surface states on large scales through molecular dynamic simulation and shows the effect of chiral Dzyaloshinskii-Moriya interaction on magnons. In addition, this work clearly elucidates the surface transport properties of Cu_3TeO_6, which provide helpful information for future studies in Cu_3TeO_6 and its application in spintronic device fabrications.

[1] Y. L. Chen, J. G. Analytis, J. H. Chu, Z. K. Liu, S. K. Mo, X. L. Qi, H. J. Zhang, D. H. Lu, X. Dai, Z. Fang, S. C. Zhang, I. R. Fisher, Z. Hussain, and Z. X. Shen, Experimental realization of a three-dimensional topological insulator, Bi_2Te_3, Science **325**, 178 (2009).

[2] D. Hsieh, D. Qian, L. Wray, Y. Xia, Y. S. Hor, R. J. Cava, and M. Z. Hasan, A topological dirac insulator in a quantum spin hall phase, Nature (London) **452**, 970 (2008).

[3] D. Hsieh, Y. Xia, L. Wray, D. Qian, A. Pal, J. H. Dil, J. Osterwalder, F. Meier, G. Bihlmayer, C. L. Kane, Y. S. Hor, R. J. Cava, and M. Z. Hasan, Observation of unconventional quantum spin textures in topological insulators, Science **323**, 919 (2009).

[4] T. Zhang, P. Cheng, X. Chen, J. F. Jia, X. C. Ma, K. He, L. L. Wang, H. J. Zhang, X. Dai, Z. Fang, X. C. Xie, and Q. K. Xue, Experimental Demonstration of Topological Surface States Protected by Time-Reversal Symmetry, Phys. Rev. Lett. **103**, 266803 (2009).

[5] X. T. Zhou, C. Fang, W. F. Tsai, and J. P. Hu, Theory of quasiparticle scattering in a two-dimensional system of helical dirac fermions: Surface band structure of a three-dimensional topological insulator, Phys. Rev. B **80**, 245317 (2009).

[6] P. Roushan, J. Seo, C. V. Parker, Y. S. Hor, D. Hsieh, D. Qian, A. Richardella, M. Z. Hasan, R. J. Cava, and A. Yazdani, Topological surface states protected from backscattering by chiral spin texture, Nature (London) **460**, 1106 (2009).

[7] M. Z. Hasan and C. L. Kane, Colloquium: Topological insulators, Rev. Mod. Phys. **82**, 3045 (2010).

[8] Y. C. Fu and H. Qin, Topological phases and bulk-edge correspondence of magnetized cold plasmas, Nat. Commun. **12**, 3924 (2021).

[9] M. G. Silveirinha, Proof of the Bulk-Edge Correspondence through a Link between Topological Photonics and Fluctuation-Electrodynamics, Phys. Rev. X **9**, 011037 (2019).

[10] C. Fang, L. Lu, J. W. Liu, and L. Fu, Topological semimetals with helicoid surface states, Nat. Phys. **12**, 936 (2016).

[11] G. Xu, H. M. Weng, Z. J. Wang, X. Dai, and Z. Fang, Chern Semimetal and the Quantized Anomalous Hall Effect in $HgCr_2Se_4$, Phys. Rev. Lett. **107**, 186806 (2011).

[12] A. A. Burkov and L. Balents, Weyl Semimetal in a Topological Insulator Multilayer, Phys. Rev. Lett. **107**, 127205 (2011).

[13] C. Fang, M. J. Gilbert, X. Dai, and B. A. Bernevig, Multi-Weyl Topological Semimetals Stabilized by Point Group Symmetry, Phys. Rev. Lett. **108**, 266802 (2012).

[14] J. P. Liu and D. Vanderbilt, Weyl semimetals from noncentrosymmetric topological insulators, Phys. Rev. B **90**, 155316 (2014).

[15] B. J. Yang and N. Nagaosa, Classification of stable three-dimensional Dirac semimetals with nontrivial topology, Nat. Commun. **5**, 4898 (2014).

[16] S. M. Young, S. Zaheer, J. C. Y. Teo, C. L. Kane, E. J. Mele, and A. M. Rappe, Dirac Semimetal in Three Dimensions, Phys. Rev. Lett. **108**, 140405 (2012).

[17] H. M. Weng, C. Fang, Z. Fang, B. A. Bernevig, and X. Dai, Weyl Semimetal Phase in Noncentrosymmetric Transition-Metal Monophosphides, Phys. Rev. X **5**, 011029 (2015).

[18] K. Mullen, B. Uchoa, and D. T. Glatzhofer, Line of Dirac Nodes in Hyperhoneycomb Lattices, Phys. Rev. Lett. **115**, 026403 (2015).

[19] C. Fang, Y. G. Chen, H. Y. Kee, and L. Fu, Topological nodal line semimetals with and without spin-orbital coupling, Phys. Rev. B **92**, 081201(R) (2015).

[20] L. X. Yang, Z. K. Liu, Y. Sun, H. Peng, H. F. Yang, T. Zhang, B. Zhou, Y. Zhang, Y. F. Guo, M. Rahn, D. Prabhakaran, Z. Hussain, S. K. Mo, C. Felser, B. Yan, and Y. L. Chen, Weyl semimetal phase in the non-centrosymmetric compound taas, Nat. Phys. **11**, 728 (2015).

[21] S. Y. Xu, I. Belopolski, N. Alidoust, M. Neupane, G. Bian, C. L. Zhang, R. Sankar, G. Q. Chang, Z. J. Yuan, C. C. Lee, S. M. Huang, H. Zheng, J. Ma, D. S. Sanchez, B. K. Wang, A. Bansil, F. C. Chou, P. P. Shibayev, H. Lin, S. Jia, and M. Z. Hasan, Discovery of a Weyl fermion semimetal and topological fermi arcs, Science **349**, 613 (2015).

[22] S. Y. Xu, I. Belopolski, D. S. Sanchez, M. Neupane, G. Q. Chang, K. Yaji, Z. J. Yuan, C. L. Zhang, K. Kuroda, G. Bian, C. Guo, H. Lu, T. R. Chang, N. Alidoust, H. Zheng, C. C. Lee, S. M. Huang, C. H. Hsu, H. T. Jeng, A. Bansil, T. Neupert, F. Komori, T. Kondo, S. Shin, H. Lin, S. Jia, and M. Z. Hasan, Spin Polarization and Texture of the Fermi Arcs in the Weyl Fermion Semimetal Taas, Phys. Rev. Lett. **116**, 096801 (2016).

[23] B. Q. Lv, H. M. Weng, B. B. Fu, X. P. Wang, H. Miao, J. Ma, P. Richard, X. C. Huang, L. X. Zhao, G. F. Chen, Z. Fang, X. Dai, T. Qian, and H. Ding, Experimental Discovery of Weyl Semimetal TaAs, Phys. Rev. X **5**, 031013 (2015).

[24] K. Kuroda, M. Ye, A. Kimura, S. V. Eremeev, E. E. Krasovskii, E. V. Chulkov, Y. Ueda, K. Miyamoto, T. Okuda, K. Shimada, H. Namatame, and M. Taniguchi, Experimental Realization of a Three-Dimensional Topological Insulator Phase in Ternary Chalcogenide TlBiSe$_2$, Phys. Rev. Lett. **105**, 146801 (2010).

[25] R. Yu, H. M. Weng, Z. Fang, X. Dai, and X. Hu, Topological Node-Line Semimetal and Dirac Semimetal State in Antiperovskite Cu$_3$PdN, Phys. Rev. Lett. **115**, 036807 (2015).

[26] H. M. Weng, Y. Y. Liang, Q. N. Xu, R. Yu, Z. Fang, X. Dai, and Y. Kawazoe, Topological node-line semimetal in three-dimensional graphene networks, Phys. Rev. B **92**, 045108 (2015).

[27] S. Wang, B. C. Lin, A. Q. Wang, D. P. Yu, and Z. M. Liao, Quantum transport in Dirac and Weyl semimetals: A review, Adv. Phys.: X **2**, 518 (2017).

[28] A. C. Potter, I. Kimchi, and A. Vishwanath, Quantum oscillations from surface Fermi arcs in Weyl and Dirac semimetals, Nat. Commun. **5**, 5161 (2014).

[29] B. C. Lin, S. Wang, A. Q. Wang, Y. Li, R. R. Li, K. Xia, D. P. Yu, and Z. M. Liao, Electric Control of Fermi Arc Spin Transport in Individual Topological Semimetal Nanowires, Phys. Rev. Lett. **124**, 116802 (2020).

[30] E. V. Gorbar, V. A. Miransky, I. A. Shovkovy, and P. O. Sukhachov, Origin of dissipative Fermi arc transport in Weyl semimetals, Phys. Rev. B **93**, 235127 (2016).

[31] Y. G. Chen, Y. M. Lu, and H. Y. Kee, Topological crystalline metal in orthorhombic perovskite iridates, Nat. Commun. **6**, 6593 (2015).

[32] Y. J. Chen, L. X. Xu, J. H. Li, Y. W. Li, C. F. Zhang, H. Li, Y. Wu, A. J. Liang, C. Chen, S. W. Jung, C. Cacho, H. Y. Wang, Y. H. Mao, S. Liu, M. X. Wang, Y. F. Guo, Y. Xu, Z. K. Liu, L. X. Yang, and Y. L. Chen, Topological Electronic Structure and Its Temperature Evolution in Antiferromagnetic Topological Insulator MnBi$_2$Te$_4$, Phys. Rev. X **9**, 041040 (2019).

[33] K. Holtgrewe, C. Hogan, and S. Sanna, Evolution of topological surface states following sb layer adsorption on Bi$_2$Se$_3$, Materials **14**, 1763 (2021).

[34] Y. Kim, B. J. Wieder, C. L. Kane, and A. M. Rappe, Dirac Line Nodes in Inversion-Symmetric Crystals, Phys. Rev. Lett. **115**, 036806 (2015).

[35] M. Phillips and V. Aji, Tunable line node semimetals, Phys. Rev. B **90**, 115111 (2014).

[36] L. P. Ye, C. Y. Qiu, M. Xiao, T. Z. Li, J. Du, M. Z. Ke, and Z. Y. Liu, Topological dislocation modes in three-dimensional acoustic topological insulators, Nat. Commun. **13**, 508 (2022).

[37] Q. Wang, H. R. Xue, B. L. Zhang, and Y. D. Chong, Observation of Protected Photonic Edge States Induced by Real-Space Topological Lattice Defects, Phys. Rev. Lett. **124**, 243602 (2020).

[38] Z. X. Qian and G. Vignale, Dynamical exchange-correlation potentials for an electron liquid, Phys. Rev. B **65**, 235121 (2002).

[39] L. Lu, L. Fu, J. D. Joannopoulos, and M. Soljacic, Weyl points and line nodes in gyroid photonic crystals, Nat. Photonics **7**, 294 (2013).

[40] L. Y. Wang, S. K. Jian, and H. Yao, Topological photonic crystal with equifrequency weyl points, Phys. Rev. A **93**, 061801(R) (2016).

[41] O. Stenull, C. L. Kane, and T. C. Lubensky, Topological Phonons and Weyl Lines in Three Dimensions, Phys. Rev. Lett. **117**, 068001 (2016).

[42] S. A. Owerre, A first theoretical realization of honeycomb topological magnon insulator, J. Phys.: Condens. Matter **28**, 386001 (2016).

[43] D. Wang, X. Y. Bo, F. Tang, and X. G. Wan, Calculated magnetic exchange interactions in the Dirac magnon material Cu$_3$TeO$_6$, Phys. Rev. B **99**, 035160 (2019).

[44] F. Y. Li, Y. D. Li, Y. B. Kim, L. Balents, Y. Yu, and G. Chen, Weyl magnons in breathing pyrochlore antiferromagnets, Nat. Commun. **7**, 12691 (2016).

[45] M. F. Lapa, G. Y. Cho, and T. L. Hughes, Bosonic analog of a topological Dirac semimetal: Effective theory, neighboring phases, and wire construction, Phys. Rev. B **94**, 245110 (2016).

[46] J. Fransson, A. M. Black-Schaffer, and A. V. Balatsky, Magnon Dirac materials, Phys. Rev. B **94**, 075401 (2016).

[47] W. L. Yao, C. Y. Li, L. C. Wang, S. J. Xue, Y. Dan, K. Iida, K. Kamazawa, K. K. Li, C. Fang, and Y. Li, Topological spin excitations in a three-dimensional antiferromagnet, Nat. Phys. **14**, 1011 (2018).

[48] H. Kondo and Y. Akagi, Nonlinear magnon spin nernst effect in antiferromagnets and strain-tunable pure spin current, Phys. Rev. Res. **4**, 013186 (2022).

[49] R. Matsumoto and S. Murakami, Rotational motion of magnons and the thermal hall effect, Phys. Rev. B **84**, 184406 (2011).

[50] R. Matsumoto and S. Murakami, Theoretical Prediction of a Rotating Magnon Wave Packet in Ferromagnets, Phys. Rev. Lett. **106**, 197202 (2011).

[51] Y. Onose, T. Ideue, H. Katsura, Y. Shiomi, N. Nagaosa, and Y. Tokura, Observation of the magnon hall effect, Science **329**, 297 (2010).

[52] M. Herak, H. Berger, M. Prester, M. Miljak, I. Zivkovic, O. Milat, D. Drobac, S. Popovic, and O. Zaharko, Novel spin lattice in Cu_3TeO_6: An antiferromagnetic order and domain dynamics, J. Phys.: Condens. Matter **17**, 7667 (2005).

[53] K. Y. Choi, P. Lemmens, E. S. Choi, and H. Berger, Lattice anomalies and magnetic excitations of the spin web compound Cu_3TeO_6, J. Phys.: Condens. Matter **20**, 505214 (2008).

[54] S. H. Baek, H. W. Yeo, J. Park, K. Y. Choi, and B. Buchner, Unusual spin pseudogap behavior in the spin web lattice Cu_3TeO_6 probed by te-125 nuclear magnetic resonance, Phys. Rev. Res. **3**, 033109 (2021).

[55] K. K. Li, C. Y. Li, J. P. Hu, Y. Li, and C. Fang, Dirac and Nodal Line Magnons in Three-Dimensional Antiferromagnets, Phys. Rev. Lett. **119**, 247202 (2017).

[56] I. Dzyaloshinsky, A thermodynamic theory of weak ferromagnetism of antiferromagnetics, J. Phys. Chem. Solids **4**, 241 (1958).

[57] T. Moriya, Anisotropic superexchange interaction and weak ferromagnetism, Phys. Rev. **120**, 91 (1960).

[58] V. Kisiček, D. Dominko, M. čulo, Ž. Rapljenović, M. Kuveždić, M. Dragičević, H. Berger, M. Herak, and T. Ivek, Linear magnetoelectric effect in topological antiferromagnet Cu_3TeO_6, arXiv:2211.08902.

[59] R. Cheng, S. Okamoto, and D. Xiao, Spin Nernst Effect of Magnons in Collinear Antiferromagnets, Phys. Rev. Lett. **117**, 217202 (2016).

[60] V. A. Zyuzin and A. A. Kovalev, Magnon Spin Nernst Effect in Antiferromagnets, Phys. Rev. Lett. **117**, 217203 (2016).

[61] See Supplemental Material at http://link.aps.org/supplemental/10.1103/PhysRevB.108.094427 for detailed results of calculations in bulk band structures, and surface arc states in Cu_3TeO_6.

[62] L. H. Thomas, The motion of the spinning electron, Nature (London) **117**, 514 (1926).

[63] P. Nyborg, Thomas precession and classical theories of spinning particles, Nuovo Cimento **23**, 1057 (1962).

[64] I. P. Omelyan, I. M. Mryglod, and R. Folk, Algorithm for Molecular Dynamics Simulations of Spin Liquids, Phys. Rev. Lett. **86**, 898 (2001).

[65] J. P. Perdew, Generalized gradient approximations for exchange and correlation: A look backward and forward, Phys. B: Condens. Matter **172**, 1 (1991).

[66] J. Tranchida, S. J. Plimpton, P. Thibaudeau, and A. P. Thompson, Massively parallel symplectic algorithm for coupled magnetic spin dynamics and molecular dynamics, J. Comput. Phys. **372**, 406 (2018).

[67] A. A. Kovalev and V. Zyuzin, Spin torque and Nernst effects in Dzyaloshinskii-Moriya ferromagnets, Phys. Rev. B **93**, 161106 (2016).

[68] H. T. Zhang and R. Cheng, A perspective on magnon spin nernst effect in antiferromagnets, Appl. Phys. Lett. **120**, 090502 (2022).

[69] S. Toth and B. Lake, Linear spin wave theory for single-q incommensurate magnetic structures, J. Phys.: Condens. Matter **27**, 166002 (2015).

[70] W. J. Jiang, P. Upadhyaya, Y. B. Fan, J. Zhao, M. S. Wang, L. T. Chang, M. R. Lang, K. L. Wong, M. Lewis, Y. T. Lin, J. S. Tang, S. Cherepov, X. Z. Zhou, Y. Tserkovnyak, R. N. Schwartz, and K. L. Wang, Direct Imaging of Thermally Driven Domain Wall Motion in Magnetic Insulators, Phys. Rev. Lett. **110**, 177202 (2013).

[71] M. Weiler, M. Althammer, M. Schreier, J. Lotze, M. Pernpeintner, S. Meyer, H. Huebl, R. Gross, A. Kamra, J. Xiao, Y. T. Chen, H. J. Jiao, G. E. W. Bauer, and S. T. B. Goennenwein, Experimental Test of the Spin Mixing Interface Conductivity Concept, Phys. Rev. Lett. **111**, 176601 (2013).

[72] M. Y. Wong, C. Y. Tso, T. C. Ho, and H. H. Lee, A review of state of the art thermal diodes and their potential applications, Int. J. Heat Mass Transf. **164**, 120607 (2021).

[73] X. Q. Wu, L. P. He, Y. Hou, X. C. Tian, and X. L. Zhao, Advances in passive check valve piezoelectric pumps, Sensors and Actuators A: Physical **323**, 112647 (2021).

[74] P. Zeng, L. Li, J. S. Dong, G. M. Cheng, J. W. Kan, and F. Xu, Structure design and experimental study on single-bimorph double-acting check-valve piezoelectric pump, Proc. Inst. Mech. Eng., Part C: J. Mech. Eng. Sci. **230**, 2339 (2016).

[75] L. Chen, M. E. Boulanger, Z. C. Wang, F. Tafti, and L. Taillefer, Large phonon thermal hall conductivity in the antiferromagnetic insulator Cu_3TeO_6, Proc. Nat. Acad. Sci. USA **119**, e2208016119 (2022).